Introduction of High-Valent Metal in Transition Metal Layer as a Structural Reinforcement for a O3-Type $NaCrO_2$ Sodium-Ion Battery Cathode

Gwangeon Oh, Jun Tae Kim, Heesung Shin, Shivam Kansara, Hyokyeong Kang, Jun Pyo Son, Yoon Seok Jung, Dominic Bresser, Shiyu Li,* Hun-Gi Jung,* and Jang-Yeon Hwang**

O3-type layered sodium chromium oxide (O3-$NaCrO_2$) is a promising cathode material for cost-effective and practical sodium-ion batteries (SIBs). However, achieving a high energy density in SIBs with $NaCrO_2$ as the cathode remains challenging owing to chromium migration and irreversible phase transition at voltages above 3.6 V (vs Na/Na^+). Herein, a substantially improved high-voltage stability of O3-$NaCrO_2$ (O3-NCO) as a cathode through the implementation of high-valent Nb^{5+} substitution strategies is reported. The strong interaction between Nb^{5+} and O^{2-} ions alleviates structural stress during repeated charge and discharge processes. The introduced Nb^{5+} enhances the disorder in the transition metal layer and structural stability, increasing the reversibility by suppressing Cr disproportionation reactions and irreversible Cr migration. Additionally, Nb^{5+} creates Na^+/vacancies in the Na layer owing to charge compensation, thereby facilitating the Na-ion diffusion kinetics. Consequently, 3 mol% of Nb-substituted O3-$Na_{0.94}Cr_{0.97}Nb_{0.03}O_2$ cathode demonstrates superior reversible capacity, cycle life, and rate capability. Furthermore, the high-valent Nb substitution strategy improves water stability and shows good compatibility with all-solid-state battery systems, highlighting its excellent practical applicability.

1. Introduction

Amid escalating concerns over climate change and carbon emissions, secondary batteries have emerged as key enablers of the global clean energy transition.[1,2] They play a pivotal role in diverse sectors, ranging from electric vehicles (EVs) and renewable energy storage systems to grid-stabilization technologies.[3] Among these, lithium-ion batteries (LIBs) currently dominate owing to their high energy density and long cycle life, particularly for EV applications.[4,5] However, the growing demand for LIBs has raised concerns regarding the long-term sustainability of lithium resources, highlighting the need to explore alternative chemistries that offer comparable performance with improved resource abundance and supply chain security.[6,7] Sodium-ion batteries (SIBs) are attracting increasing interest as a promising

---

G. Oh, J. T. Kim, H. Shin, S. Kansara, H. Kang, S. Li, J.-Y. Hwang
Department of Energy Engineering
Hanyang University
Seoul 04763, Republic of Korea
E-mail: Li-SY@henu.edu.cn; jangyeonhw@hanyang.ac.kr

J. T. Kim, H.-G. Jung
Energy Storage Research Center
Sustainable Energy Research Division
Korea Institute of Science and Technology
Seoul 02792, Republic of Korea
E-mail: hungi@kist.re.kr

J. P. Son, Y. S. Jung
Department of Chemical and Biomolecular Engineering
Yonsei University
Seoul 03722, Republic of Korea

The ORCID identification number(s) for the author(s) of this article can be found under https://doi.org/10.1002/sstr.202500400.

DOI: 10.1002/sstr.202500400

Y. S. Jung
Department of Battery Engineering
Yonsei University
Seoul 03722, Republic of Korea

D. Bresser
Helmholtz Institute Ulm (HIU)
Helmholtzstrasse 11, 89801 Ulm, Germany
E-mail: dominic.bresser@kit.edu

D. Bresser
Karlsruhe Institute of Technology (KIT)
P.O. Box 3640, 76021 Karlsruhe, Germany

S. Li
Henan Key Laboratory of High Efficiency Energy Conversion Science and Technology
Henan International Joint Laboratory of New Energy Materials and Devices
School of Physics and Electronics
Henan University
Kaifeng 475004, P. R. China

H.-G. Jung
KIST-SKKU Carbon-Neutral Research Center
Sungkyunkwan University
Suwon 16419, Republic of Korea

alternative for large-scale, intermittent grid-energy storage owing to the natural abundance of sodium and its chemical similarity to lithium.[8–10] However, the larger ionic radius of Na^+ (1.02 Å) compared with Li^+ (0.76 Å) poses significant challenges to structural stability, often resulting in increased internal resistance and sluggish Na^+ diffusion kinetics.[11] Additionally, the higher atomic weight and less negative redox potential of sodium (22.99 g mol^{-1}, –2.73 V vs Na^+/Na) relative to lithium (6.94 g mol^{-1}, –3.04 V vs Li^+/Li) limit the achievable gravimetric energy density.[11] For the commercial viability of SIBs, careful design and optimization of the active materials are critical, particularly with respect to cathodes, which play a decisive role in determining energy density, cycling stability, and rate performance. In this context, layered transition metal (TM) oxides have garnered significant attention, inspired by their successful application in LIBs.[12] Therefore, research on layered cathode materials tailored for SIBs has become a central focus for advancing next-generation battery technologies.[13]

Among O3-type layered TM oxides (Na_xTMO_2, where TM = Ti, V, Cr, Ni, Co, Fe, Mn, etc.), O3-$NaCrO_2$ stands out as a promising cathode material for SIBs owing to its high theoretical capacity of ≈240 mAh g^{-1} when utilizing 1 mol of Na^+.[14–17] Despite this advantage, $NaCrO_2$ suffers from severe capacity fading, particularly when more than 0.5 mol of Na^+ is extracted, primarily owing to irreversible structural transitions at high voltages.[18] At voltages above 3.8 V (corresponding to $x > 0.5$ in $Na_{1-x}CrO_2$), Cr^{4+} ions tend to undergo disproportionation reactions ($3Cr^{4+}(3d^2) \rightarrow 2Cr^{3+}(3d^3) + Cr^{6+}(3d^0)$), particularly in regions with concentrated Cr^{4+}–Cr^{4+}–Cr^{4+} arrangements.[19] The resulting Cr^{6+}, characterized by an empty 3d orbital configuration ($3d^0$), preferentially occupies tetrahedral sites within the Na layer rather than the octahedral sites of the TM layer. This site preference facilitates Cr^{6+} migration into the Na layer, where it subsequently engages in a comproportionate reaction with neighboring Cr^{3+} species, generating Cr^{4+} ions that become trapped in the octahedral sites in the Na layer. These Cr^{4+} ions cannot reintegrate into the TM layer, leading to the formation of oxygen vacancies and triggering an irreversible phase. Such structural degradation drastically undermines the electrochemical performance and long-term stability of the O3-$NaCrO_2$ cathode.

While limiting the extraction of Na^+ to 0.5 mol in O3-$NaCrO_2$ enables relatively stable cycling and power performance by avoiding extensive Na^+ vacancy ordering, it also induces complex phase transitions, such as to the monoclinic O′3 and P′3 phases, during the charge/discharge process.[20] From a practical standpoint, achieving higher energy density while maintaining structural stability remains a critical challenge. To mitigate the irreversible phase transitions above 3.8 V, which are strongly associated with Na^+ vacancy ordering, various strategies involving aliovalent cations and TM substitutions have been explored. For example, Obrovac et al. synthesized Ca-substituted O3-$NaCrO_2$ via a solid-state reaction. Owing to the comparable ionic radii and chemical properties of Ca^{2+} (1.00 Å) and Na^+ (1.02 Å), Ca^{2+} ions preferentially occupy sites within the sodium layer. These electrochemically inactive cations serve as structural pillars during cycling, contributing to enhanced high-voltage stability. As a result, the modified material exhibited increased reversible capacity and reduced voltage hysteresis within the 2.0–3.8 V range.[21] In another study, Chen et al. reported the substitution of Nb^{5+} into Cr^{3+} sites, which alleviated the lattice strain and facilitated Na-layer expansion.[22] The stronger Nb—O bond, relative to the Cr—O bond, contributed to the improved structural robustness during repeated cycling. Although previous studies have demonstrated the positive impact of Nb^{5+} substitution on the electrochemical performance of O3-$NaCrO_2$, a comprehensive understanding of the underlying mechanisms, particularly those related to charge compensation, local structural evolution, and their implications for practical performance, remains insufficient.

H.-G. Jung
Department of Energy Science
Sungkyunkwan University
Suwon 16419, Republic of Korea

J.-Y. Hwang
Department of Battery Engineering
Hanyang University
Seoul 04763, Republic of Korea

In this study, a series of Nb-substituted layered oxides with the general formula $Na_{1-2x}Cr_{1-x}Nb_xO_2$ (x = 0, 0.01, 0.03, and 0.05) was synthesized via a conventional solid-state reaction route. To gain comprehensive insight into the physicochemical and electrochemical roles of high-valent Nb substitution, a combined theoretical and experimental approach was employed. The results indicate that the incorporation of Nb^{5+} into the Cr^{3+} sites effectively suppresses the irreversible phase transitions typically observed in the voltage range of 1.5–3.8 V. The enhanced Nb—O bond strength relative to that of Cr–O mitigates the structural stress during cycling, while the distinct ionic radius and Fermi level of Nb^{5+} introduce increased cationic disorder in the TM layer, thereby inhibiting Cr disproportionation. Moreover, high-valent metal substitution generates vacancies for charge compensation, which leads to the expansion of the Na layer and improves the Na^+ diffusion kinetics. Among the compositions studied, $Na_{0.94}Cr_{0.97}Nb_{0.03}O_2$ (O3-NCN3O) exhibited the best electrochemical performance, with enhanced reversible capacity, superior rate capability, and excellent cycling stability. In addition to the electrochemical performance, the practical viability of O3-NCN3O was further validated by assessing its thermal and moisture stability as well as its successful integration into an all-solid-state sodium-ion battery configuration.

2. Result and Discussion

A series of $Na_{1-2x}Cr_{1-x}Nb_xO_2$ (x = 0, 0.01, 0.03, 0.05) samples was synthesized using a conventional solid-state reaction method.[23] The chemical compositions of the as-prepared samples were determined using inductively coupled plasma optical emission spectrometry (ICP-OES; Table S1, Supporting Information). Hereafter, $NaCrO_2$, $Na_{0.98}Cr_{0.99}Nb_{0.01}O_2$, $Na_{0.94}Cr_{0.97}Nb_{0.03}O_2$, and $Na_{0.90}Cr_{0.95}Nb_{0.05}O_2$ are referred to as O3-NCO, O3-NCN1O, O3-NCN3O, and O3-NCN5O, respectively. X-ray diffraction (XRD) analysis was performed using the Rietveld refinement method to investigate the crystallographic information, lattice parameters, and possible impurities of the synthesized samples. The calculated diffraction patterns and the corresponding cell parameters, along with the refinement results, are shown in **Figure 1**a,b, and S1, S2 and Table S2, Supporting information.[24] All diffraction peaks can be indexed to the simulated O3-phase crystal structure with the R-3m space group. Owing to the similar ionic radii of Cr^{3+} (0.615 Å) and Nb^{5+} (0.64 Å), Nb^{5+} ions were preferentially incorporated into the TM layers occupying the octahedral 3a Wyckoff sites. The *c*-axis lattice parameters of O3-NCO, O3-NCN1O, O3-NCN3O, and O3-NCN5O were 15.955, 15.983, 15.995, and 15.983 Å, respectively. The *c*-axis expands with increasing Nb content because Nb substitution induces Na^+ vacancies to maintain charge neutrality, thereby enhancing the repulsion force between the Na–O layers.[25] Based on the Rietveld refinement data, we can suggest that the formation of vacancies into Na sites can be attributed to Nb substitution. To confirm the existence of vacancies in Na layers of O3-NCN3O, we conducted the vacancy formation energy calculations (Figure S3, Supporting information).

In addition, the TM—O bond is strengthened owing to the larger cationic potential of Nb^{5+} compared with that of Cr^{3+}.[26] However, when Nb^{5+} substitution exceeded 5 mmol, negligible changes in the *c*-axis were observed, accompanied by the formation of a $NaNbO_3$ impurity phase, indicating the solubility limit of Nb^{5+} in the O3-NCO crystal.[27] The appearance of $NaNbO_3$ diffraction peaks is discussed in detail later.

Scanning electron microscopy (SEM) analysis was performed to examine the morphologies of O3-NCO, O3-NCN1O, O3-NCN3O, and O3-NCN5O (Figure S4, Supporting Information). The SEM images revealed that all samples were composed of plate-like primary particles with nanoscale diameters ranging from 200 to 500 nm. These observations indicate that the introduction of Nb ions has a negligible impact on particle morphology. High-resolution transmission electron microscopy (HR-TEM) was used to gain further insight into the microstructure of O3-NCN3O. As shown in Figure 1c, O3-NCN3O exhibits a high degree of crystallinity; the interplanar spacing of 1.60 nm

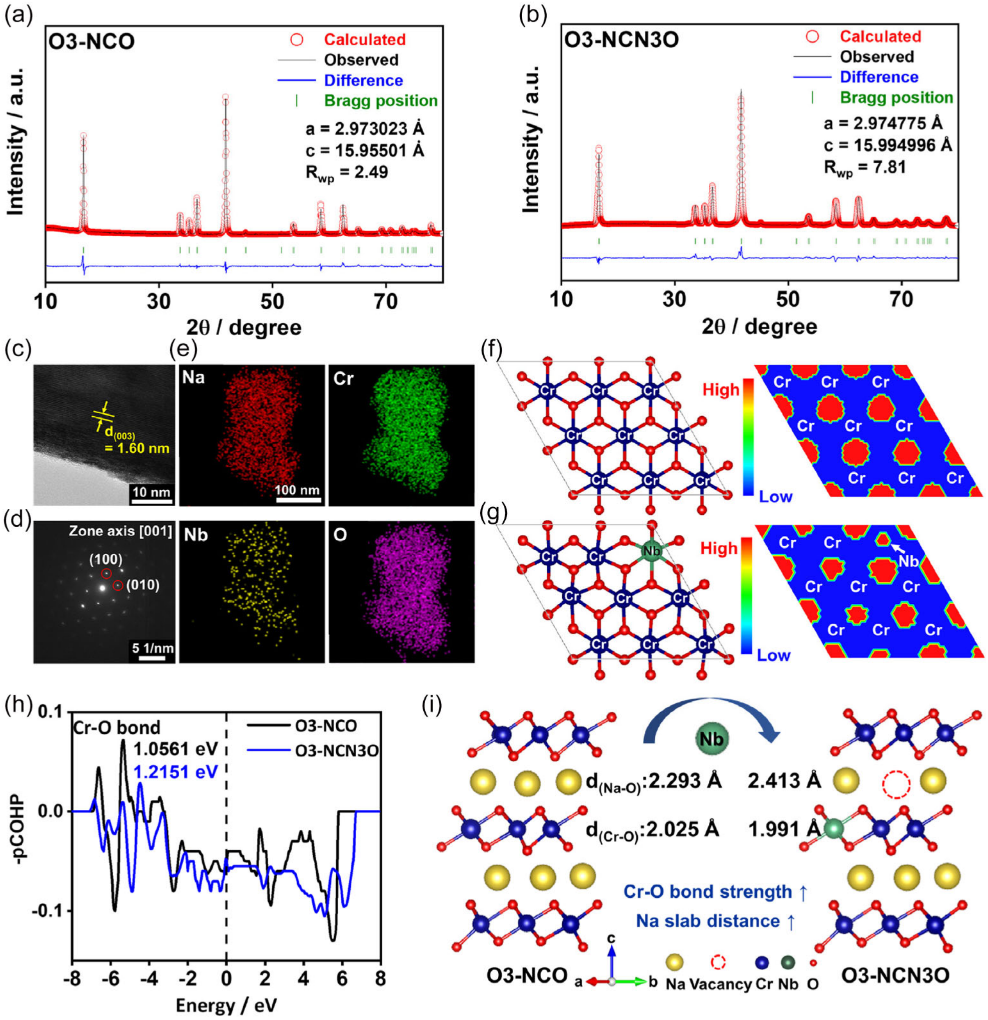

Figure 1. Rietveld refined XRD patterns of the a) O3-NCO and b) O3-NCN3O cathodes. c) HR-TEM image and d) SAED patterns of O3-NCN3O. e) Energy-dispersive X-ray spectroscopy elemental mapping of O3-NCN3O. f,g) Top-view atomic structures of O3-NCO and O3-NCN3O, respectively, with corresponding ELF maps. h,i) COHP analysis of the Cr—O bond and associated changes in the bond length for O3-NCO and O3-NCN3O, respectively, obtained from DFT calculations.

corresponds to the (003) planes of the R-3 m space group. Furthermore, a well-defined ABCABC stacking sequence of the atomic layer was observed along the [001] zone axis, further confirming the O3-type layered structure (Figure 1d). The energy-dispersive X-ray spectroscopy (EDS) mapping images revealed a uniform distribution of Na, Cr, Nb, and O in both O3-NCO and O3-NCN3O samples (Figure 1e and S5, Supporting Information).

Electron localization function (ELF) (Figure 1f,g) maps revealed how Nb substitution and Na content jointly reshaped the bonding and electrostatic landscape of Na_xCrO_2. In fully sodiated O3-NCO, ELF isosurfaces form symmetrical, high-localization lobes around each oxygen atom, signaling uniform Cr–O covalency and discrete, zero ELF lobes at the Na sites, which is consistent with purely ionic Na–O interactions that effectively screen interlayer Coulomb repulsion. By contrast, the partially desodiated, O3–NCN3O displays pronounced asymmetry in its ELF distribution: intense localization appears around the Nb—O bonds, indicating that fewer Na^+ ions remain to neutralize the negative charge on the oxide sheets, and O^{2-}–O^{2-} repulsion grows. The stronger in-plane covalent character of Nb–O driven by the high oxidation state and polarizing power of Nb^{5+} draws electron density into the TM slabs, partially offsetting the layer-separating effect of the unscreened electrostatic repulsion. This competition manifests in the vertical spacing of Cr–O lobes to adjacent Na layers: in O3-NCO, the distance is minimal, whereas in O3-NCN3O, it increases noticeably, directly visualizing the balance between enhanced M–O localization (which contracts the lattice) and amplified interlayer Coulomb repulsion (which expands it) along the z-axis (Figure S6, Supporting information). Minor distortions around the Na vacancies further modulate the local ELF, demonstrating how even a small degree of Nb substitution and Na deficiency profoundly influence both the electronic structure and lattice geometry in these layered oxides. To further elucidate the bonding nature and structural response during sodium intercalation, we conducted a crystal orbital Hamilton population (COHP) analysis of the Cr—O bond in the discharged states of NCO and NCN3O.

As shown in Figure 1h, the integrated −pCOHP value for the Cr—O bond increased from 1.0561 eV for O3-NCO to 1.2151 eV for O3-NCN3O, indicating stronger covalent interactions in the Nb-substituted structure. This enhancement can be attributed to the electronic influence of high-valent Nb^{5+}, which alters the local electronic environment and promotes stronger Cr–O hybridization. To complement this finding, we examined the bond lengths in the discharged states (Figure 1i). The average Cr—O bond distance decreases from 2.025 Å in O3-NCO to 1.991 Å in O3-NCN3O, while the Na—O bond distance slightly increases from 2.293 Å to 2.413 Å, which follows the general trend.[28] The shortening of the Cr—O bond confirms the strengthening of the TM–O interactions upon Nb^{5+} substitution. Cr—O bond shortening has two complementary effects: first, each Nb^{5+} ion introduces two extra positive charges, forcing the local lattice to compensate by creating Na^+ vacancies; and second, the empty 4 d orbitals of Nb strongly polarize adjacent O 2p electrons, boosting the partial covalent character and bond order of both the Nb–O and neighboring Cr—O bonds.

Concurrently, the increased Na–O slab spacing facilitates Na^+ migration, alleviates structural stress, and mitigates Na^+/vacancy ordering, thereby implying enhanced structural integrity that contributes to improved cycling reversibility.[28] Together, the bond length and COHP analyses provide compelling evidence that Nb substitution significantly modifies the local bonding landscape, thereby improving the structural robustness of O3-NCN3O during sodium de/intercalation. In Bader-charge analyses of the discharged phases of O3-NCO, the approximate charges for the Na, Cr, and O atoms are +0.80 |e|, +1.50 |e|, and –1.10 |e|, respectively. By comparison, the charges in O3-NCN3O slightly redistribute: the Na atoms retain their charge of +0.80 |e|, the charge of the Cr atoms decreases to +1.45 |e|, the charge of the O atoms becomes marginally more negative (–1.12 |e|), and the Nb atom charge is +2.70 |e|. Consequently, the Nb—O bonds bear ≈1.25 |e| more positive charge than the Cr—O bonds, directly reflecting the higher oxidation state of Nb and its strong polarizing effect on the oxide framework (Figure S7, Supporting information).

To further investigate the high-voltage stability of both samples, electrochemical tests were carried out within an extended voltage window of 1.5–3.8 V, compared to the conventional range of 1.5–3.6 V typically employed in previous studies.[17] The initial charge/discharge voltage profiles of all the samples at a current density of 0.1C (1C = 120 mA g^{-1}) are presented in **Figure 2**a,b and S8, Supporting information. Upon initial charging, O3-NCO, O3-NCN1O, O3-NCN3O, and O3-NCN5O exhibited specific charge capacities of 195.9, 139.5, 134.2, and 120.0 mAh g^{-1}, respectively, with O3-NCO showing the highest value owing to the extended voltage plateau near 3.8 V. However, when assessing the reversibility, O3-NCO delivers the lowest discharge capacity of 76.4 mAh g^{-1} and a Coulombic efficiency (CE) of only 39.1%, significantly lower than the Nb-substituted samples. By contrast, O3-NCN1O and O3-NCN3O demonstrated improved discharge capacities of 130.7 mAh g^{-1} and 129.8 mAh g^{-1}, with corresponding CEs of 93.7% and 96.7%, respectively. O3-NCN5O showed a slightly reduced discharge capacity of 114.1 mAh g^{-1}, attributed to the presence of the electrochemically inactive orthorhombic $NaNbO_3$ phase, which possesses low electrical and ion conductivities.[29] To further elucidate the origin of the differences in discharge capacity and CE as a function of Nb substitution, the dQ/dV profiles were derived by differentiating the first-cycle charge/discharge curves of O3-NCO and O3-NCN3O (Figure 2c,d). As shown in Figure 2c, O3-NCO undergoes a multi-stage phase-transition sequence of hexagonal O3 ($O3_{hex}$)–monoclinic O′3 ($O3_{mon}$)–monoclinic P′3 ($P3_{mon}$)–X, corresponding to several voltage plateaus observed in the charge/discharge profile.[30] A distinct oxidation peak was observed near 3.8 V, associated with the $P3_{mon}$ to X phase transition. During discharging, the corresponding reduction peak was significantly suppressed, likely owing to an irreversible phase transition occurring in the high-voltage region near 3.8 V. This irreversible transition not only accounts for the higher initial charge capacity of O3-NCO but also explains its lower discharge capacity and reduced CE. By contrast, O3-NCN3O displayed similar electrochemical characteristics to O3-NCO, except for the pronounced oxidation peak at 3.8 V (Figure 2d). Notably, all oxidation peaks in O3-NCN3O appeared reversibly as corresponding reduction peaks, which contributed to its enhanced discharge capacity and improved CE. A more detailed discussion of the phase evolution mechanism during charging and discharging is provided based on the in situ XRD analysis. The cycling performances of

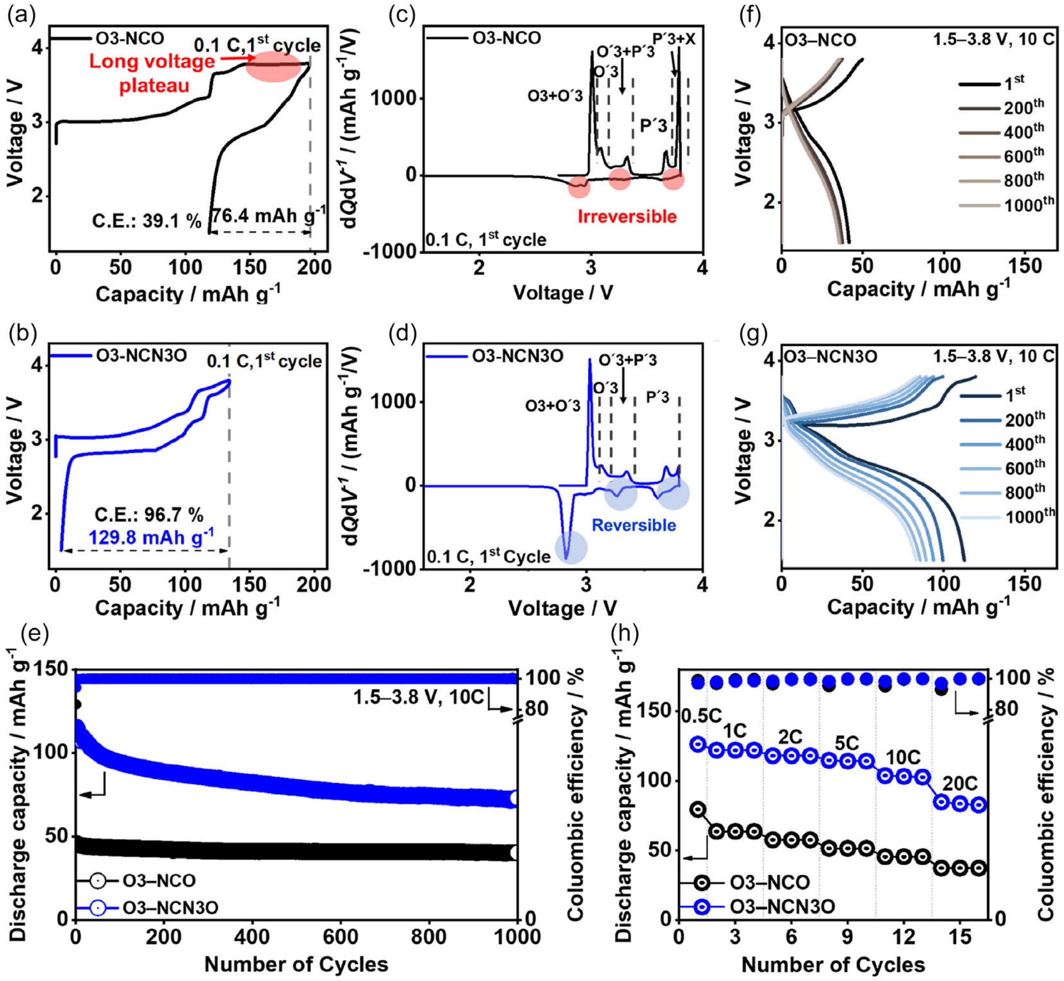

Figure 2. Initial charge and discharge profiles of a) O3-NCO and b) O3-NCN3O between 1.5 and 3.8 V at 0.1C and corresponding dQ dV^{-1} plots of c) O3-NCO and d) O3-NCN3O cathodes. e) Results of cycling tests at 10C and selected charge–discharge curves of f) O3-NCO and g) O3-NCN3O, and h) rate capabilities in the voltage range of 1.5–3.8 V at current densities of 0.5C to 20C.

both samples were evaluated at current densities of 1C and 10C (Figure 2e–g and S9–S12, Supporting Information). During cycling at 1C, the O3-NCN3O cathode exhibited the highest reversible capacity and most stable cycling behavior over 50 cycles (Figure S9 and S10, Supporting information). Moreover, under a high-rate cycling condition of 10C for 1000 cycles, O3-NCN3O demonstrated superior long-term stability with a capacity retention of 73.0 mAh g^{-1}. By contrast, the capacities of O3-NCO, O3-NCN1O, and O3-NCN5O declined to 40.4, 56.5, and 48.7 mAh g^{-1}, respectively (Figure S11 and S12, Supporting Information). The rate performances of all samples were further assessed at varying current densities ranging from 0.5 C to 20C within a voltage window of 1.5–3.8 V. Among all samples, O3-NCN3O delivered the best rate performance, achieving discharge capacities of 128.1, 122.0, 118.3, 114.1, 103.7, and 83.54 mAh g^{-1} at 0.5C, 1C, 2C, 5C, 10C, and 20C, respectively (Figure 2h and S13 and S14, Supporting information). The enhanced cycling stability and rate capability of O3-NCN3O can be attributed to the strong Nb—O bonds in the TM layer and the presence of Na$^+$ vacancies within the Na layers, which synergistically relieved structural stress and facilitated Na$^+$ diffusion during the insertion and extraction processes. To further understand the effect of high-valent Nb substitution on the reaction kinetics after the 1st and 1000th cycles at 10C, electrochemical impedance spectroscopy was conducted. The resulting Nyquist plots were fitted using the equivalent circuit model shown in Figure S15, Supporting Information. Figure S16a,b and Table S3, Supporting Information) show the Nyquist plots of the O3-NCO and O3-NCN3O electrodes in the discharged state after the 1st and 1000th cycle at 10C. The high-frequency region of the spectra was correlated with the surface diffusion resistance (R_{sei}), and the intermediate-frequency region was related to the charge transfer resistance (R_{ct}) at the electrode–electrolyte interface.[31] After the 1st cycle, O3-NCN3O exhibited significantly lower R_{sei} and R_{ct} values than O3-NCO. The lower R_{sei} is attributed to the suppression of the irreversible phase transition and the resulting structural integrity. The lower R_{ct} is attributed to the improved charge-transfer kinetics resulting from the electronic structure modified by the Nb substitution and the generation of Na$^+$ vacancies within the Na layers.

A convex-hull analysis was conducted to study the thermodynamic stability of O3-NCN3O. During Na^+ extraction, the O3-NCN3O cathode phase-transitioned from O3 to P3, helping to maintain its structural integrity and continuous Na-ion diffusion channels despite a charge of >3.8 V (**Figure 3**a). This structural adaptability, along with the favorable transport properties, is also reflected in the voltage profile, where the density functional theory (DFT)-predicted curve matches well with the experimental data, thus validating the theoretical findings (Figure 3b). The partial density of states (PDOS) results directly correlate with the electronic conductivity behavior of both the O3-NCO and O3-NCN3O systems during charge–discharge cycling, as shown in Figure 3c,d. In the case of O3-NCO, the narrow bandgap (0.19 eV in the discharged state (OCV) (full Na) indicates limited but non-negligible electronic conductivity owing to the partially occupied Cr 3 d states near the Fermi level. However, upon charging to the $Na_{0.2}CrO_2$ composition, the bandgap widens significantly to 1.07 eV. This large increase reflects the transition to a more insulating state as electrons are removed and Cr is oxidized, which suppresses the charge carrier density and reduces the electronic conductivity in the desodiated phase. By contrast, O3-NCN3O exhibits superior electronic characteristics. The OCV state (for $Na_{0.94}$) exhibited an even narrower band gap of 0.113 eV, indicating an enhanced intrinsic conductivity compared with that of O3-NCO. This improvement can be attributed to the electronic contribution of the Nb 4d states, which partially overlap with the O 2p orbitals near the Fermi level and introduce additional conducting channels. When charged to $Na_{0.4}Cr_{0.97}Nb_{0.03}O_2$, the band gap only increases to 0.70 eV still considerably lower than that of charged NCO implying that the Nb dopant mitigates the drop in conductivity typically observed upon desodiation. The Na-ion migration profiles further demonstrate the advantages of O3-NCN3O using climbing image-nudged elastic band (CI-NEB). As shown in Figure 3e,f, the activation energy barriers for Na diffusion were lower in NCN3O across both the discharged and charged states. At OCV, the barrier drops slightly from 0.88 eV in NCO to 0.80 eV in NCN3O, indicating marginal improvement. However, the impact of Nb-doping becomes much more significant upon charging: while NCO exhibits a high migration barrier of 0.928 eV, the barrier in NCN3O drops dramatically to just 0.29 eV. The enhanced electronic conductivity facilitated by

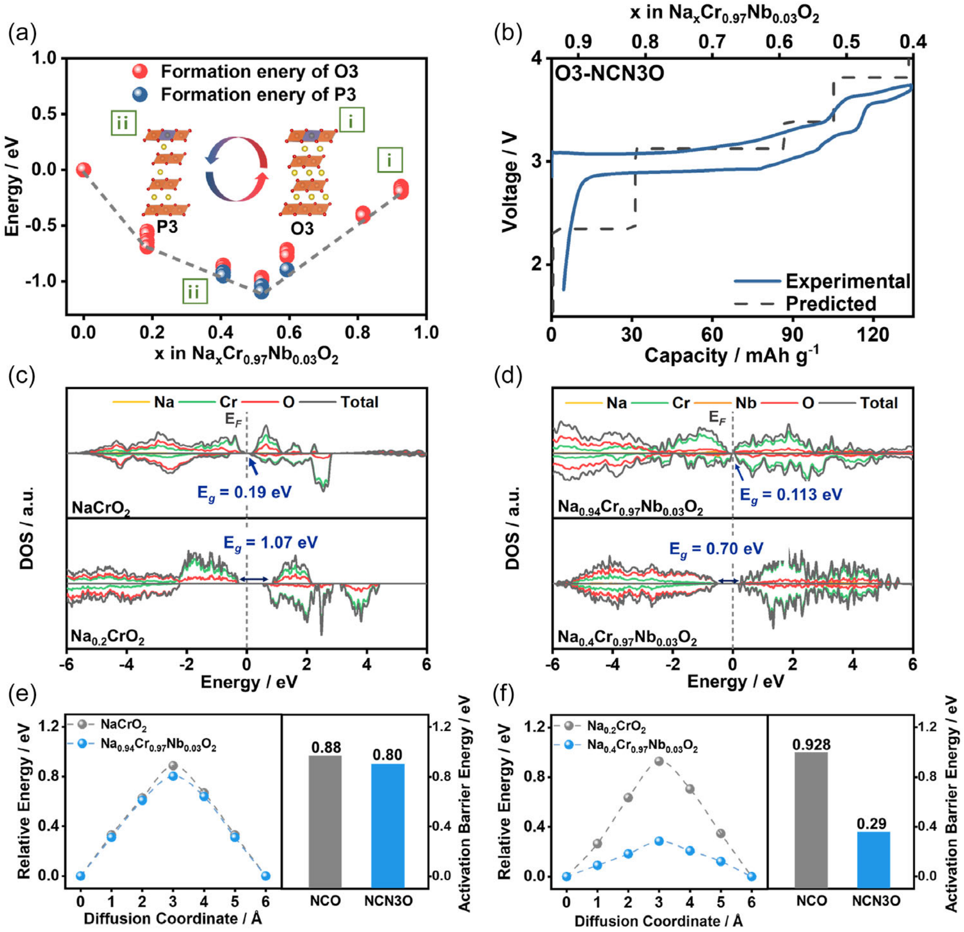

Figure 3. a) Convex-hull plot of various O3-/P3-$Na_x[Cr_{0.94}Nb_{0.03}]O_2$ configurations ($0.4 \leq x \leq 0.94$) with theoretical redox potentials. b) Comparison of experimentally obtained charge-discharge curves with voltage profiles predicted from first-principles calculations. c,d) PDOS plots of the discharged and charged states of O3-NCO and O3-NCN3O. e,f) Calculated relative energies associated with the Na^+ migration pathways in O3-NCO and O3-NCN3O, respectively.

the presence of Nb through additional Nb–O contributions near the Fermi level complements the significantly lower Na-ion migration barrier (0.29 eV) observed in the charged NCN3O structure, as shown in Figure S17, Supporting information. In addition to OCV and charged state of NEB calculation, to directly compare Na^+ migration energetics at equivalent sodiation levels, we performed CI-NEB calculations on both O3- and P3-type configurations at $x \approx 0.93$, 0.82, 0.52, and 0.40 (plus an additional O3 point at $x \approx 0.20$ for NCO) in O3-NCN3O and O3-NCO (Figure S18, supporting information). In each case, the highest energy barrier in NCN3O is substantially lower than in NCO e.g., 0.80 eV versus 0.86 eV at $x \approx 0.93$, 0.76 eV versus 0.82 eV at $x \approx 0.82$, 0.29 eV versus 0.33 eV at $x \approx 0.52$, and 0.25 eV versus 0.37 eV at $x \approx 0.4$ demonstrating that Nb^{5+} substitution consistently smooths the Na^+ migration pathway across both O3 and P3 phases. This systematic reduction in barrier height confirms that the combined effects of enhanced M–O covalency and increased vacancy concentration in NCN3O lower the activation energy for Na^+ hopping at all intermediate compositions. The concurrent decreases in migration barrier, the resulting diffusivity proportional to the product of vacancy concentration and the Arrhenius factor rise by more than three orders of magnitude, offering a quantitative explanation for the faster Na^+ transport observed experimentally in NCN3O.

Ex situ X-ray absorption near edge structure (XANES) measurements were conducted at the Cr K-edge to investigate the local structure and oxidation state of Cr in O3-NCO and O3-NCN3O during cycling. **Figure 4**a–c presents the XANES spectra of the pristine O3-NCO and O3-NCN3O samples, along with Cr_2O_3 and CrO_3 reference compounds, representing Cr^{3+} and Cr^{6+} oxidation states, respectively. As shown in Figure 4a, the pristine electrodes of both O3-NCO and O3-NCN3O exhibit absorption edge

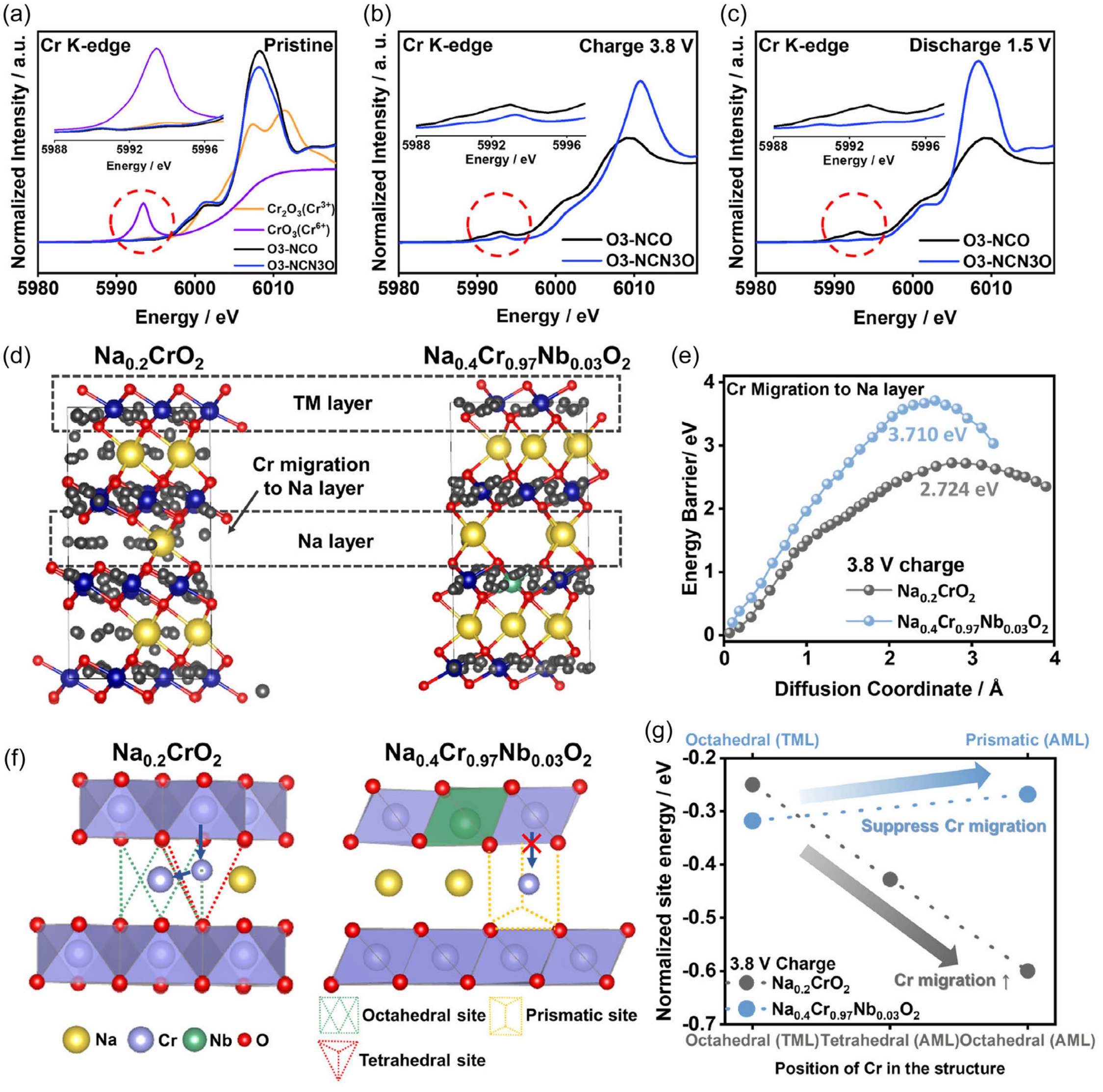

Figure 4. Cr K-edge XANES spectra of O3-NCO and O3-NCN3O cathode in various states; a) pristine state, b) charged state (3.8 V), and c) discharged state (1.5 V). d) Schematic illustration of possible Cr ion migration pathways. e) Corresponding energy barriers for Cr migration. f,g) BVPA models showing possible Cr migration sites and their associated normalized site energies under the charged states of the cathodes.

positions consistent with that of Cr^{3+}, confirming that Cr exists predominantly in the 3+ oxidation state in the as-prepared materials. This observation also supports the successful substitution of Nb^{5+} into the TM sites without altering the initial oxidation state of Cr, in accordance with the ICP-OES results (Table S1, Supporting information). Upon charging to 3.8 V (Figure 4b), a clear shift of the Cr K-edge to a higher energy was observed, indicating the oxidation of Cr^{3+} to Cr^{4+} as Na^+ was extracted from the structure.[32] Notably, when more than 0.5 mol of Na^+ was removed, the Cr^{4+} ions underwent the following disproportionation reaction[19]

$$3Cr^{4+}(3d_2) \rightarrow 2Cr^{3+}(3d_3) + Cr^{6+}(3d_0) \tag{1}$$

This disproportionation highlights a critical instability in the high-voltage regime. Consequently, a pronounced increase in the pre-edge feature at 5992 eV was observed in the Cr K-edge XANES spectrum. This enhancement is indicative of the presence of Cr^{6+}, as evidenced by comparison with the strong pre-edge signal of CrO_3. The origin of this feature is attributed to the formation of tetrahedrally coordinated Cr^{6+} species, which allows an electric dipole-allowed transition from the 1s to hybridized p–d orbitals, thereby intensifying the pre-edge signal.[33] Notably, the O3-NCO sample exhibited a stronger pre-edge peak than O3-NCN3O, indicating a higher fraction of Cr^{6+} in O3-NCO (Figure 4b). This can be ascribed to the extended voltage plateau near 3.8 V in O3-NCO, which promoted the formation of Cr^{4+} and facilitated the Cr disproportionation reaction.[18] By contrast, O3-NCN3O does not exhibit a significant plateau in the same region, indicating suppressed Cr disproportionation. This suppression was attributed to the presence of a strong Nb—O bond in the TM layers, which enhanced the structural stability and inhibited the undesired phase transitions associated with Cr migration. Moreover, the incorporation of Nb^{5+} disrupted the ordering of the TM layers, thereby reducing the likelihood of Cr disproportionation reactions. Upon discharge, the O3-NCN3O sample displays a pre-edge peak with both positions and intensities nearly identical to those of the pristine state, indicating a highly reversible $Cr^{3+/4+}$ redox process during cycling (Figure 4c). By contrast, the O3-NCO electrode retained an elevated pre-edge peak intensity after discharging, indicating incomplete reversibility. This behavior was attributed to the irreversible migration of Cr ions from the TM layers to the more thermodynamically stable tetrahedral sites within the Na layer. Once Cr^{6+} ions migrate into these sites, they become kinetically trapped and cannot readily return to the TM layers during the discharge process.[30] These findings highlight that Nb^{5+} substitution in O3-NCN3O effectively stabilizes the TM layer, suppresses detrimental Cr migration, and enables a more reversible redox reaction, thereby contributing to its superior electrochemical performance.

To investigate the resilience of the Cr framework to disorder during 3.8 V charging, we examined two different migration pathways for a Cr ion to move from its native octahedral site in the TM layer to sites within the alkali metal (Na) layer of O3-NCO ($Na_{0.2}$) and P3-NCN3O ($Na_{0.4}$), as low sodiation affects the structural phase, based on the DFT analysis. Figure 4d illustrates these pathways schematically (gray spheres mark possible Cr positions) using Bond Valence Pathway Analyzer (BVPA) and plots the corresponding energy barriers at 3.8 V charge: in pure $Na_{0.2}CrO_2$ (left), Cr can hop into either a tetrahedral site alkali metal layer (AML) or an octahedral site in the Na layer (AML) from an octahedral site (TM layer (TML)), but the highest barrier for completing that path is 2.724 eV (Figure 4e). By contrast, in $N_{0.4}Cr_{0.97}Nb_{0.03}O_2$ (right), the only feasible migration channel is from the octahedral site (TML) to the prismatic site in the Na layer (AML) and that barrier rises even higher, and the barrier increases to 3.710 eV (Figure 4e), showing that Nb substitution and the P3 stacking pattern together strongly suppress Cr movement. To understand why these barriers differed, we calculated the site energy of a Cr atom lodged at each candidate site, relative to its native octahedral position (Figure 4f). For $Na_{0.2}CrO_2$ (3.8 V charged state), three destinations were considered: octahedral vacancies in the TML, tetrahedral vacancies in the Na layer (AML), and octahedral vacancies in the Na layer (AML). In $Na_{0.2}CrO_2$ (Figure 4g), moving Cr to an AML site is substantially more favorable than relocating it to a TML site. By contrast, for $Na_{0.4}Cr_{0.97}Nb_{0.03}O_2$ (3.8 V charged state), the only local minimum outside the original octahedral site is the prismatic Na-layer environment. Its energy lies only slightly above the TM-layer octahedral level, while all other positions (including any hypothetical tetrahedral or octahedral Na-layer sites) are far too high in energy to be occupied. Physically, this means the prismatic geometry of P3 stacking and the stronger, more directional M—O bonds imparted by Nb^{5+} leave no low-energy stepping stones for Cr to wander into the Na layers. Chemically, these results reflect two key factors: 1) the high-valent Nb ion pulls electron density into the TM-layer bonds, making them stronger and less likely to break, and 2) P3 stacking changes the coordination geometry in the Na layer to a prismatic site that is intrinsically less hospitable to a Cr^{6+} ion. Together, these effects increase the cost of the Cr migration energy barrier compared to that of the unsubstituted $Na_{0.2}CrO_2$ structure, explaining why high-valent Nb-substituted $Na_{0.4}Cr_{0.97}Nb_{0.03}O_2$ exhibits far greater reversibility under high-voltage cycling.

To elucidate the structural evolution during Na^+ (de)insertion, in situ XRD analysis was performed during the first charge-discharge of O3-NCO and O3-NCN3O within the voltage range of 1.5–3.8 V at a current density of 0.1C. **Figure 5**a,b displays the contour plots of selected 2θ regions: 15°–18°, 31°–38°, 40°–43°, 43°–47°, and 60°–65°. Upon charging, both the (003) and (006) reflections shifted toward lower angles, indicating a single-phase solid-solution reaction characterized by the expansion of the *c*-axis.[34] This expansion resulted from the increased electrostatic repulsion between O^{2-} ions owing to Na^+ extraction. Concurrently, the (101) and (012) reflections shift to higher angles, indicating that the oxidation of Cr ions decreases their average ionic radius in the transition metal layers, thereby contracting the *a*-axis. At ≈3.1 V, the emergence of the monoclinic O′3 phase is observed, evidenced by the splitting and shifting of the (003), (012), and (104) peaks, indicating lattice distortion from the original hexagonal O3 structure.[18] As charging proceeds to 3.3 V, the O′3 phase gradually diminishes, while the monoclinic P′3 phase becomes predominant. Both O3-NCO and O3-NCN3O undergo an O3-O′3-P′3 phase transition during charging, however, notable differences appear at the fully charged state near 3.8 V. For O3-NCO, the P′3 phase reflection around 15° abruptly disappears, consistent with previous reports

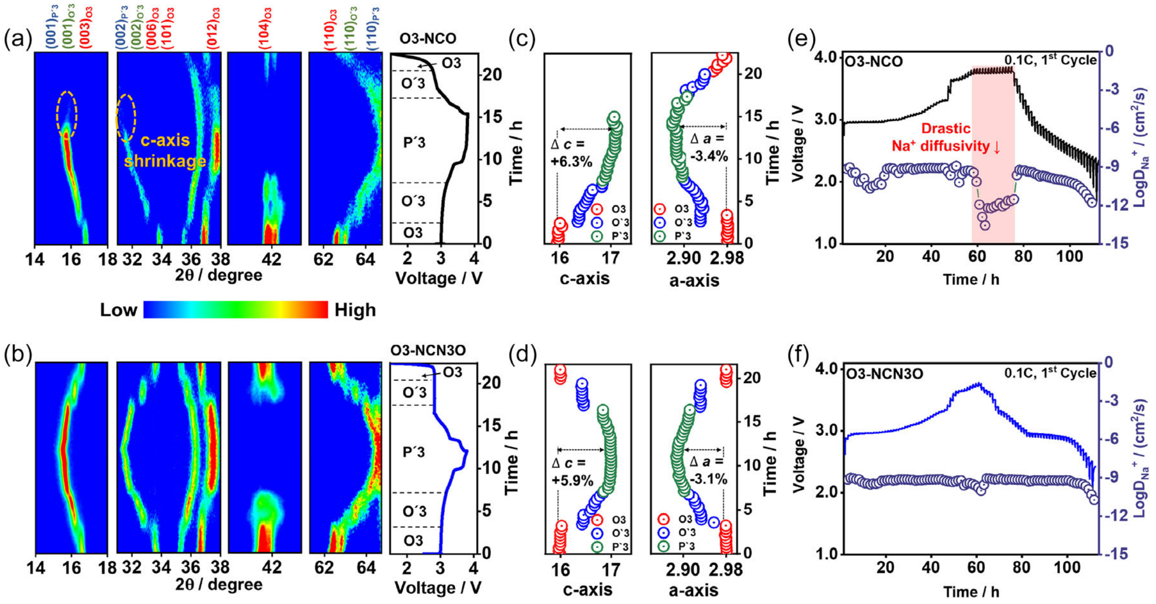

Figure 5. In situ XRD patterns of the a) O3–NCO and b) O3–NCN3O cathodes obtained during the first-cycle galvanostatic charge and discharge profiles. The lattice parameter changes along the *c*- and *a*-axes during the first charge and discharge, derived from in situ XRD analysis, are shown for c) O3–NCO and d) O3–NCN3O. GITT curves with Na^+ diffusion coefficient at 1st cycle of e) O3-NCO and f) O3-NCN3O.

on $NaCrO_2$ cathodes at highly charged states. By contrast, O3-NCN3O exhibits continuous Na^+ extraction at the end of the charging process, while maintaining the P′3 phase. Upon discharging to 1.5 V, O3-NCN3O reversibly returns to the hexagonal O3 phase via the monoclinic O′3 phase, whereas O3-NCO fails to undergo a reversible phase transition. This behavior correlates with the disappearance of the P′3 peak at the end of the charged state. In the high-voltage region, a Cr disproportionation reaction occurred when more than 0.5 mol of Na^+ was extracted. Cr^{6+}, which is thermodynamically favored at tetrahedral sites within the Na layer, readily migrates into the Na layers.[35] The resulting TM vacancies, induced by Cr migration trigger an oxygen release, leading to the formation of an X-phase with a rapidly contracting lattice to achieve thermodynamic stability. By contrast, the introduction of Nb^{5+} strengthened the bonding within the TM layer and increased the degree of cationic disorder, effectively suppressing Cr disproportionation and undesirable Cr-ion migration. This stabilization enabled the retention of the P′3 phase without abrupt (003) plan shrinkage at the end of charging. These results are consistent with the XANES analysis and Cr migration energy calculations. Further analysis of lattice parameter variations during electrochemical cycling (Figure 5c,d) reveals that O3-NCN3O exhibits smaller changes in both the *c*- and *a*-axes than O3-NCO (O3-NCO: Δ*a*: −3.4%, Δ*c*: +6.3%, O3-NCN3O: Δ*a*: −3.1%, Δ*c*: +5.9%). This reduced lattice distortion is attributed to the stronger Nb—O bonds than Cr—O bonds, which alleviate structural stress and result in more stable lattice parameters throughout cycling. This finding is consistent with the superior long-term cycling stability shown in Figure 2e.

To investigate the Na^+ transport kinetics in a certain voltage region of O3-NCO and O3-NCN3O, galvanostatic intermittent titration technique (GITT) measurements were performed. The GITT tests were conducted during the first charge/discharge cycle, applying a constant current pulse of 0.1 C for 15 min, followed by a 1-hour relaxation period, within a voltage range of 1.5–3.8 V.[36] For both samples, the sodium-ion diffusion coefficient, D_{Na^+}, was calculated based on Fick's second law using the following expression

$$D_{Na^+} = \frac{4}{\pi\tau}\left(\frac{n_m V_m}{S}\right)^2\left(\frac{\Delta E_S}{\Delta E_t}\right)^2 \tag{2}$$

where τ is the duration of the current pulse (s), n_m is the amount of active material (mol), V_m is the molar volume of the electrode material ($cm^3\ mol^{-1}$), S denotes the electrode–electrolyte contact area (cm^2), ΔE_s is the steady-state voltage changes during the relaxation period, and ΔE_τ is the transient voltage change during the constant current pulse. The GITT curves and corresponding D_{Na^+} values for O3-NCO and O3-NCN3O are presented in Figure 5e,f. For O3-NCO, the D_{Na^+} values ranged from $1.2 \times 10^{-10}\ cm^2\ s^{-1}$ to $2.82 \times 10^{-14}\ cm^2\ s^{-1}$, with an average value of $9.03 \times 10^{-11}\ cm^2\ s^{-1}$. By contrast, O3-NCN3O exhibited an enhanced average D_{Na^+} value of $4.57 \times 10^{-10}\ cm^2\ s^{-1}$, ranging from $9.12 \times 10^{-10}\ cm^2\ s^{-1}$ to $1.95 \times 10^{-11}\ cm^2\ s^{-1}$. The improved Na^+ diffusion kinetics in O3-NCN3O are attributed to the Nb substitution, which effectively suppressed the irreversible phase transition near 3.8 V, thereby enhancing the high-voltage stability and reversibility. Furthermore, the strong Nb—O bonds and the introduction of Na^+ vacancies reduced the charge transfer resistance during the charge/discharge process, leading to an increase in the average D_{Na^+} and suppression of the large fluctuation typically observed during cycling.

To further investigate the structural and chemical stability of the cathode materials after prolonged cycling, the TEM coupled with fast Fourier transform analysis and X-ray photo spectroscopy (XPS) was performed on the O3-NCO and O3-NCN3O electrodes after 1000 cycles at 10C. As shown in Figure S19a,b, Supporting information, both samples were examined for surface and structural degradation. The TEM image of the cycled O3-NCO cathode reveals a structurally deformed, ≈5–10 nm thick surface layer, indicating pronounced surface deterioration. By contrast, the O3-NCN3O samples exhibit thinner and, more uniform surface layers, indicating improved surface integrity. The presence of an amorphous layer on the outermost region of both samples, delineated by yellow dotted lines (Figure S19a,b Supporting information), is attributed to hydrofluoric acid (HF) attack from electrolyte decomposition.[37] HR-TEM confirmed that the layered structure of O3-NCO was significantly damaged, which is consistent with the large unit cell volume fluctuations and irreversible phase transitions observed in the in situ XRD analysis.[38] Conversely, the O3-NCN3O cathode retained its layered structure with minimal structural disruption, indicating its superior resilience to long-term cycling.

To assess the chemical stability of the electrodes after long-term cycling, XPS was performed on the O3-NCO and O3-NCN3O electrodes after 1000 cycles at 10C. In addition, to elucidate the correlation between the enhanced structural stability with high reversibility and its impact on electrolyte decomposition, the surfaces of O3-NCO and O3-NCN3O (end of discharge at the 1000th cycle at 10C) were analyzed using XPS. In particular, the F 1s XPS spectra provide insights into the decomposition behavior of the $NaPF_6$ salt and fluoroethylene carbonate (FEC) additive. The degradation of $NaPF_6$ typically follows a stepwise process:[37]

$$NaPF_6 \rightarrow NaF + PF_5 \tag{3}$$

$$PF_5 + H_2O \rightarrow POF_3 + 2HF \tag{4}$$

$$2POF_3 + 3Na_2O \rightarrow 6NaF + P_2O_5 \tag{5}$$

The F 1s XPS spectra were deconvoluted into three distinct peaks corresponding to Na–F (685.2 eV), $Na_xPO_yF_z$ (686.8 eV), and C–F (688.3 eV), as shown in Figure S20, Supporting information.[39] For all three components, the O3-NCO cathode exhibited significantly higher peak intensities than O3-NCN3O, indicating a greater extent of electrolyte salt decomposition.[40] Additionally, the C 1s XPS spectra revealed strong signals associated with C—C, C═O, C—O, and C—F species, which are attributed to the decomposition of the EC and DEC solvents (Figure S21, Supporting information).[41] Notably, the O3-NCO sample displayed a higher concentration of organic decomposition products than O3-NCN3O. These findings are consistent with the more severe electrolyte degradation inferred from the F1s spectra and further highlight the superior interfacial stability of the Nb-substituted O3-NCN3O cathode. To deeper investigation into Nb-induced changes in surface chemistry, we conducted oxygen vacancy energy calculation of O3-NCO and O3-NCN3O. We have to check vacancy energy of O from surface of O3-NCO and O3-NCN3O. $\Delta E_{vac} = E(slab–O) + ½E(O_2) – E(slab)$. ΔE_{vac} increases from 1.52 eV in pristine to 2.10 eV in the Nb-substituted surface (Figure S22 and S23, Supporting information). By strengthening the local M—O bonds (particularly Nb—O), Nb substitution makes it thermodynamically less favorable for surface oxygen to be removed a key first step in electrolyte oxidation.

Figure S24, Supporting information presents the Cr 2p spectra of the O3-NCO and O3-NCN3O electrodes after extended cycling, highlighting the evolution of the chromium oxidation states. A noticeably higher proportion of Cr^{4+} species was detected in the O3-NCO cathode, indicative of irreversible redox behavior associated with Cr migration and structural instability under high-voltage operation (1.5–3.8 V).[30] This elevated Cr^{4+} content was sustained over prolonged cycling, reflecting the persistent nature of these parasitic reactions. By contrast, the O3-NCN3O electrode displays a significantly lower Cr^{4+} contribution, even after repeated cycling, indicating that Nb^{5+} substitution effectively stabilizes the local electronic structure by suppressing the Cr disproportionation and migration phenomena. This stabilization is consistent with the mitigated lattice distortions observed in the XANES and in situ XRD analysis. Complementary TEM and XPS characterizations further confirm that Nb incorporation reinforces structural robustness and reduces electrolyte-induced surface degradation at high potentials, thereby underpinning the superior cycling performance of O3-NCN3O.

From practical perspective, the moisture sensitivity of the cathode materials remains a critical challenge for the commercialization of SIBs. Brief exposure to ambient humidity can initiate Na^+/H^+ ion exchange at the particle surface, leading to the formation of insulating byproducts such as Na_2CO_3, NaOH, and $NaHCO_3$, which severely compromise electrochemical performance.[42] To assess the water tolerance of the synthesized materials, both O3-NCO and O3-NCN3O samples were immersed in deionized water for 10 min, followed by vacuum drying at 100 °C overnight.[43] The corresponding XRD patterns are shown in **Figure 6**a,b. For the O3-NCO sample, pronounced structural degradation was observed after water exposure, which was attributed to extensive Na^+ extraction that destabilized the layered framework and promoted the formation of $NaHCO_3$ impurities.[44] By contrast, O3-NCN3O maintained its layered structure with only trace amounts of $NaHCO_3$, indicating superior structural resilience. This enhanced water stability is ascribed to Nb^{5+} substitution in the TM layer, which reinforces the host framework and effectively mitigates Na^+/H^+. Additionally, the generation of Na^+ vacancies in the Na layers owing to high-valent Nb^{5+} doping further suppresses surface reactions with moisture.[45] To further elucidate the impact of moisture exposure on electrochemical performance, both samples were subjected to post-treatment cycling. Figure 6c,d presents the initial charge–discharge profiles of water-exposed O3–NCO and O3–NCN3O cathodes, tested at 0.1 C within a voltage window of 1.5–3.8 V. The O3–NCN3O electrode delivered an initial discharge capacity of 108.8 mAh g^{-1} with a CE of 86.3%, while O3–NCO showed a substantially lower discharge capacity of 69.7 mAh g^{-1} and a significantly reduced CE of 47.4%, indicative of irreversible side reactions and active material degradation. As illustrated in Figure 6e, the O3-NCN3O electrode retained a discharge capacity of 53.1 mAh g^{-1} after 100 cycles at 1C, corresponding to 63% capacity retention, thereby demonstrating excellent structural and electrochemical stability under moisture stress. In stark contrast, the O3-NCO electrode exhibited rapid capacity decay, retaining only 12.3 mAh g^{-1} after 100 cycles. This pronounced degradation is attributed to structural collapse and surface

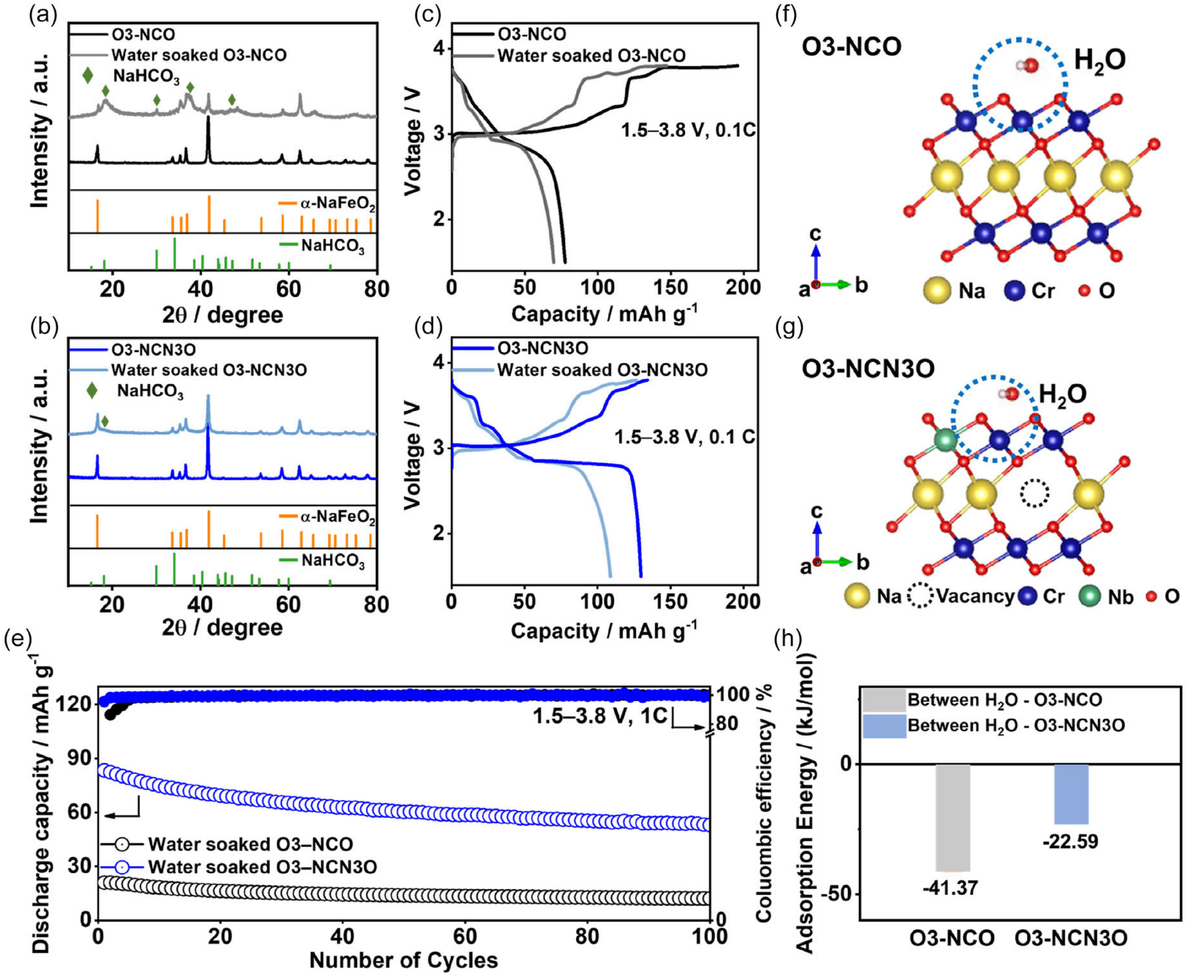

Figure 6. Water stability of the O3-NCO and O3-NCN3O samples. XRD patterns of a) O3-NCO and b) O3-NCN3O before and after soaking in water for 10 min. Charge and discharge profiles before and after soaking in water for c) O3-NCO and d) O3-NCN3O. e) Cycle stability of O3-NCO and O3-NCN3O after water soaking. H_2O absorption models of f) O3-NCO and g) O3-NCN3O. h) Binding energies for H_2O absorption for both samples.

passivation by insulating byproducts such as $NaHCO_3$, which hinder Na^+ transport and electrode kinetics.

Using DFT, we studied the molecular adsorption of water onto O3-NCO and O3-NCN3O in two ways: a surface absorption reaction and an interlayer H_2O insertion reaction, as depicted in Figure 6f–h and S25 (Supporting information). Figure 6f,g shows the schematic illustrations of the adsorbed H_2O molecules on the O3-NCO and O3-NCN3O surface, respectively. Water binding on the exposed surface is exothermic, with adsorption energies of $-41.37\,\text{kJ mol}^{-1}$ on NCO and $-22.59\,\text{kJ mol}^{-1}$ on O3-NCN3O. The surface oxygens on O3-NCO act as strong Lewis bases, readily forming hydrogen bonds and stabilizing the water molecule, whereas the Nb-induced polarization of the O 2p electrons in O3-NCN3O reduces this basicity and weakens surface interactions. Consequently, O3-NCO wets more easily, whereas O3-NCN3O offers greater resistance to surface hydration. The case of H_2O molecule insertion into the O3-NCO and O3-NCN3O is shown in Figure S25, Supporting information. When a single water molecule is inserted between the oxide layers, the process becomes endothermic, requiring $8.19\,\text{kJ mol}^{-1}$ of O3-NCO and a substantially higher $80.17\,\text{kJ mol}^{-1}$ of O3-NCN3O. This energy cost reflects the need to separate negatively charged O^{2-} sheets and overcome their mutual repulsion an effect that is greatly amplified by Nb^{5+} substitution, strengthening the in-plane M—O bonds and tightening the layer spacing, leaving fewer sites for water to occupy. These DFT calculation results indicate that Nb substitution significantly enhanced the water resistivity of the O3-NCO cathode.

In addition to liquid electrolyte system, we also confirm the practical feasibility of O3-NCN3O in the all-solid-state-batteries (ASSBs). ASSBs configured as cathode composite (O3-NCN3O–Na_2O_2–$ZrCl_4$–carbon)|Na_2O_2–$ZrCl_4$|Na_3PS_4|Na_3Sn were fabricated and subsequently evaluated. Na_2O_2-$ZrCl_4$, which is electrochemically stable within the operating voltage range of O3-NCN3O and exhibits high ionic conductivity, was employed as the primary solid electrolyte in the cell.[46] To mitigate potential interfacial reactions with the Na_3Sn anode, Na_3PS_4 was introduced as an interlayer. The XRD patterns for the obtained Na_2O_2-$ZrCl_4$ and Na_3PS_4 are shown in Figure S26, Supporting information.[46,47] The SEM images revealed that Na_2O_2-$ZrCl_4$ and

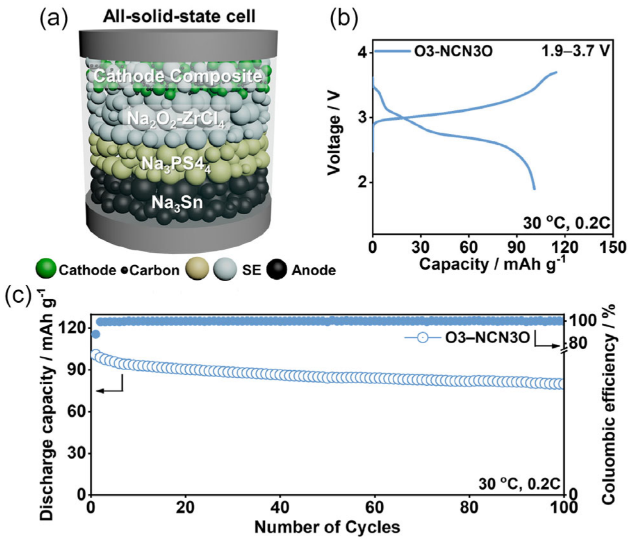

Figure 7. Electrochemical performance of all-solid-state cells incorporating the O3-NCN3O cathode. a) Schematic illustration of the O3-NCN3O-SE|Na_2O_2-$ZrCl_4$|Na_3PS_4|Na_3Sn, SE = Na_2O_2-$ZrCl_4$ all-solid-state cells. b) Initial charge and discharge curves of the O3-NCN3O all-solid-state cells at 0.2C. c) Long-term cycling stability of O3-NCN3O at 0.2C and 30 °C.

Na_3PS_4 solid electrolyte showed microscale diameters ranging from $3 \approx 5$ µm (Figure S27, Supporting information). **Figure 7**a shows a schematic of the all-solid-state cell configuration using an O3-NCN3O cathode. Electrochemical performance was assessed in the voltage range of 1.9–3.7 V at a current density of 0.2C with 30 °C (Figure 7b,c). The initial specific discharge capacity of the O3–NCN3O cathode was 100.94 mAh g^{-1}, with an initial CE of 88.2% (Figure 7b). Furthermore, the long-term cycling performance of the all-solid-state cell with O3–NCN3O demonstrated remarkable stability. After 100 cycles, the all-solid-state cell with O3-NCN3O retained 80.0% of its initial capacity, corresponding to a specific discharge capacity of ≈79.9 mAh g^{-1}, with CE approaching 100%, as depicted in Figure 7c.

3. Conclusion

In summary, a niobium substitution strategy was employed to mitigate the irreversible phase transitions typically observed in O3-type $NaCrO_2$ (O3-NCO) cathodes within the voltage window of 1.5–3.8 V. The modified O3-NCN3O cathode exhibited markedly enhanced electrochemical performance, delivering a high reversible capacity of 129.8 mAh g^{-1} with a coulombic efficiency of 96.7%, excellent capacity retention of 64% over 1000 cycles at 10C, and a strong rate capability of 84.9 mAh g^{-1} at 20C. These improvements are attributed to three primary factors: 1) suppression of the Cr^{4+} disproportionation reaction and inhibition of irreversible Cr migration by disrupting the TM layer ordering and stabilizing the structure at high voltage through high-valent Nb^{5+} incorporation; 2) improved structural robustness owing to the stronger Nb-O bonding interaction relative to Cr–O; and 3) enhanced Na^+ transport kinetics enabled by the introduction of Na^+ vacancies through high-valent Nb^{5+} substitution. In addition, the O3-NCN3O cathode demonstrated excellent resistance to moisture-induced degradation and was compatible with all-solid state sodium battery configurations, reinforcing its potential for practical deployment. These findings offer valuable design principles for engineering high-performance, structurally stable Na-ion cathode materials.

4. Experimental Section

Material Synthesis: The O3-NCO, O3-NCN1O, O3-NCN3O, and O3-NCN5O were synthesized by simple heat treatment. Cr_2O_3 (Sigma-Aldrich, 98%), Nb_2O_5 (Sigma-Aldrich, 99.99%), and Na_2CO_3 (Sigma-Aldrich, 99.5%) were used as start material. They were mixed in mortar and pestle in right stoichiometry. After mixing the start material, mixed powder was pelleted. The pelleted powder was annealed in a tube furnace at 900 °C 12 h in Ar atmosphere. The final powder was obtained by grinding the annealed powder. The O3-NCO and Nb-substituted O3-NCO cathodes were synthesized in stoichiometric proportions using Cr_2O_3, Nb_2O_5, and Na_2CO_3 as starting materials. The precursor powders were thoroughly mixed using mortar and pestle, and the resulting mixture was pelletized. The pellets were then annealed in a tube furnace at 900 °C for 12 h under Ar atmosphere. After annealing, the materials were ground into fine powders to obtain the final cathode samples. Na_2O_2-$ZrCl_4$ powders were prepared by ball milling a stoichiometric mixture of Na_2O_2 (Sigma-Aldrich, 97%) and $ZrCl_4$ (Sigma-Aldrich, 99.99%) at 500 rpm for 10 h using a Pulverisette 7 PL (Fritsch GmbH). The milling was conducted in an 80 mL ZrO_2 vial containing 15 ZrO_2 balls ($\Phi = 10$ mm). Na_3PS_4 powders were prepared by ball milling a stoichiometric mixture of Na_2S (Sigma-Aldrich, 98%) and P_2S_5 (Sigma-Aldrich, 99%) at 300 rpm for 3 h using a Pulverisette 7 PL (Fritsch GmbH), followed by heat treatment at 270 °C for 1 h in a fused-glass ampoule sealed under vacuum. Na_3Sn was prepared by manually mixing Na metal (Sigma-Aldrich, 99.9%) and Sn powder (Alfa Aesar, spherical, APS ≈ 0.1 micron) in a mortar.

Material Characterization: The structure of the final powder was identified by using XRD (SmartLab, Rigaku) with Cu Kα radiation. The morphology of the powders was observed via SEM (Helios, FEI). The composition of each sample was confirmed by using inductively coupled plasma-optical emission spectrometry (ICP-OES) (iCAP 700 SERIES, Thermo Fisher Scientific). X-ray spectroscopy (XPS) (XPS – Theta Probe, Thermo Fisher Scientific) was used to identify the surface of the electrode after cycle. Transmission electron microscopy (TEM) (NEO ARM, JEOL) was also used to identify the structure and EDS mapping. The structural evolution during cycling was acquired by in situ XRD by using a diffractometer (Empyrean, PANalytical) with a Mo Kα radiation source ($\lambda = 0.0709$ nm, Power: 60 kV, 30 mA) over a 2θ range of 4.6°–34.5°. To investigate oxidation state of O3-NCO and O3-NCN3O at pristine, charge state(3.8 V), discharge state(1.5 V), XANES measurements were conducted at the 7D beamline of the Pohang Light Source. The structural characteristic after cycling was examined by using Brucker D8 advanced in the 2θ range between 10° and 80° at 40 KV and 30 mA with a Cu Kα radiation source. TEM, selected area electron diffraction (SAED) patterns, and EDS were performed. To obtain TEM, SAED pattern, and EDS, as prepared and after cycling electrode were polished by focused ion beam (Helios, FEI).

Electrochemical Measurements: The cathode was prepared by mixing the active material, conductive carbon (Super P:KS6 = 1:1, wt%), and polyvinylidene fluoride with a ratio of 8:1:1 in N-methyl-pyrrolidone (NMP). After mixing slurry, slurry was then coated on the aluminum foil with carbon-coated layer and dried at 110 °C for 12 h to eliminate every moisture in electrode. The foil was pressed between stainless steel roller to make it uniform. The coin-type cell (CR–2032) was fabricated to test electrochemical property in glove box. The CR–2032 was assembled by cathode, sodium metal anode which was separated by polymer polyethylene separator (Celgard 2400) and glass fiber (GB-100 R). 1M $NaPF_6$ in a mixture of ethylene carbonate and diethyl carbonate (EC:DEC, 1:1 in volume ratio) with 5 wt% fluoroethylene carbonate was used as electrolyte, which was purchased from Enchem Engineering. The fabricated cells were cycled at 10C in 1.5–3.8V, 1C = 120 mA g^{-1}.

For all-solid-state half-cells, Na_3Sn was used as counter electrodes. Na_2O_2-$ZrCl_4$ powder (150 mg) was pelletized at 100 MPa to form solid electrolyte (SE) layers. To reduce interfacial reactivity between Na_2O_2-$ZrCl_4$ and Na_3Sn, an interlayer was introduced by placing a thin layer of Na_3PS_4 (50 mg) beneath the Na_2O_2-$ZrCl_4$ layer, followed by pelletization at 100 MPa. The composite working electrodes (composite cathode) were prepared by mixing O3-NCN3O, Na_2O_2-$ZrCl_4$, and super C65 powders in a weight ratio of 50:50:3 using a mortar and pestle for 15 min. The working and Na_3Sn counter electrodes were placed on each side of the SE layers, and the cell assembly was pressed at 370 MPa at room temperature. The mass loading of cathode electrode was 11.3 mg cm^{-2}. The all-solid-state cells were tested under an external pressure of 70 MPa at 30 °C.

Computational Details: All calculations in this study were conducted using the Vienna ab initio Simulation Package (VASP) code,[48] with the exchange-correlation energy described by the Perdew–Burke–Ernzerhof functional within the generalized gradient approximation framework. The projector augmented wave method was utilized to accurately model the interactions between ion nuclei and valence electrons.[49] To account for intra-atomic Coulombic repulsion, Hubbard corrections were applied using a U parameter of 3.7 and 4 eV specifically for the Cr-3d and Nb-4d electrons, respectively, thereby improving the accuracy of electron–electron interaction modeling. Moreover, spin polarization was considered in all calculations. Also, DFT + D3 was implemented during all adsorption calculations. The cut-off energies for the plane-wave expansion were set at 450 eV, and the force convergence criterion for the relaxation was 0.06 eV Å^{-1}. Also, $4 \times 4 \times 2$ Monkhorst-Pack k-point grid was employed for structural optimization, while a denser $6 \times 6 \times 2$ grid was used for all rest of calculations. A unit cell comprising 26 Cr, 54 O, and 1 Nb atoms was considered for investigating the energies associated with various configurations involving the incorporation of Na ions in NCN3O structure. To calculate the minimum energy path and the corresponding relative migration energy barriers for Na and Cr diffusion in the NCO and NCN3O structures, the CI-NEB[50] and BVPA[51] method were used. To extract chemical bonding information within the structures, LOBSTER software[52] was incorporated. In the end, we employed the VESTA software for post-processing tasks, such as analyzing structural design, and visualizing electronic properties. Formation energy and voltage calculation have been used same formulation as described in the previous reported work.[53]

Supporting Information

Supporting Information is available from the Wiley Online Library or from the author.

Acknowledgements

G.O., J.T.K., H.S., and S.K. contributed equally to this work. This research was supported by the National Research Foundation of Korea funded by the Ministry of Science and ICT of Korea (RS-2024-00408156) and Korea Evaluation Instituted of Industrial Technology (KEIT) grant funded by the korea government (MOTIE) (RS-2024-00406080). This research was supported by the Federal Ministry for Economic Affairs and Energy; BMWE; 03EI4080C.

Conflict of Interest

The authors declare no conflict of interest.

Author Contributions

Gwangeon Oh: conceptualization (lead); data curation (lead); investigation (equal); writing—original draft (lead). **Jun Tae Kim**: data curation (equal); formal analysis (lead); writing—original draft (equal). **Heesung Shin**: conceptualization (equal); data curation (lead); investigation (equal); writing—original draft (equal). **Shivam Kansara**: investigation (equal); methodology (lead); writing—original draft (equal); writing—review and editing (lead). **Hyokyeong Kang**: validation (equal); writing—original draft (equal). **Jun Pyo Son**: formal analysis (equal); writing—original draft (equal). **Yoon Seok Jung**: writing—original draft (equal); writing—review and editing (equal). **Dominic Bresser**: data curation (equal); methodology (equal); writing—original draft (equal); writing—review and editing (lead). **Shiyu Li**: writing—original draft (equal); writing—review and editing (lead). **Hun-Gi Jung**: formal analysis (equal); visualization (lead); writing—original draft (lead); writing—review and editing (equal). **Jang-Yeon Hwang**: conceptualization (lead); formal analysis (lead); supervision (lead); writing—original draft (lead); writing—review and editing (lead).

Data Availability Statement

The data that support the findings of this study are available from the corresponding author upon reasonable request.

Keywords

high power, high-valent metal substitution, high voltages, layered-type cathode, Na-ion batteries

Received: June 17, 2025
Revised: August 1, 2025
Published online:

---

[1] R. Wanison, W. N. H. Syahputra, N. K. Lue, P. Sakulchangsatjatai, C. Chaichana, V. U. Shankar, P. Suttakul, Y. Mona, *J. Energy Storage* **2024**, *100*, 113497.
[2] M. M. Hasan, R. Haque, M. I. Jahirul, M. G. Rasul, I. M. R. Fattah, N. M. S. Hassan, M. Mofijur, *J. Energy Storage* **2025**, *120*, 116511.
[3] G. G. Njema, R. B. O. Ouma, J. K. Kibet, *J. Renew. Energy* **2024**, *1*, 2329261.
[4] R. Schmuch, R. Wagner, G. Hörpel, T. Placke, M. Winter, *Nat. Energy* **2018**, *3*, 267.
[5] J. Xu, X. Cai, S. Cai, Y. Shao, C. Hu, S. Lu, S. Ding, *Energy Environ. Mater.* **2023**, *6*, e12450.
[6] V. G. Pol, *ACS Energy Lett.* **2025**, *10*, 2553.
[7] P. Christmann, E. Gloaguen, J.-F. Labbé, J. Melleton, P. Piantone, *Lith. Process Chem.* **2015**, 1, https://doi.org/10.1016/B978-0-12-801417-2.00001-3.
[8] X. Liang, J.-Y. Hwang, Y.-K. Sun, *Adv. Energy Mater.* **2023**, *13*, 2301975.
[9] H. S. Hirsh, Y. Li, D. H. S. Tan, M. Zhang, E. Zhao, Y. S. Meng, *Adv. Energy Mater.* **2020**, *10*, 2001274.
[10] K. Chayambuka, G. Mulder, D. L. Danilov, P. H. L. Notten, *Adv. Energy Mater.* **2020**, *10*, 2001310.
[11] J.-Y. Hwang, S.-T. Myung, Y.-K. Sun, *Chem. Soc. Rev.* **2017**, *47*, 3529.
[12] T. Kim, W. Song, D.-Y. Son, L. K. Ono, Y. Qi, *J. Mater. Chem. A* **2019**, *7*, 2942.
[13] Y.-J. Guo, R.-X. Jim, M. Fan, W.-P. Wang, S. Xin, L.-J. Wan, Y.-G. Guo, *Chem. Soc. Rev.* **2024**, *53*, 7828.
[14] S.-H. Choe, C.-J. Yu, J.-C. Ri, U.-G. Jong, Y.-H. Kye, S.-N. Hong, *Phys. Chem. Chem. Phys.* **2019**, *21*, 8408.

[15] M. Guignard, C. Didier, J. Darriet, P. Bordet, E. Elkaïm, C. Delmas, *Nature Materials* **2013**, *12*, 74.
[16] L. Tong, P. Ma, J. Shu, L. Wang, G. Chen, J. Wu, Y. Mi, X. Zhao, *Phys. Chem. Chem. Phys.* **2022**, *24*, 13201.
[17] C.-Y. Yu, J.-S. Park, H.-G. Jung, K.-Y. Chung, D. Aurbach, Y.-K. Sun, S.-T. Myung, *Energy Environ. Sci.* **2015**, *8*, 2019.
[18] K. Kubota, I. Ikeuchi, T. Nakayama, C. Takei, N. Yabuuchi, H. Shiiba, M. Nakayama, S. Komaba, *J. Phys. Chem. C* **2015**, *119*, 166.
[19] C. L. Jakobsen, B. P. Andersen, M. Johansen, C. K. Christensen, A. Ø. Drejer, M. A. Karlsen, D. B. Ravnsbbaek, *J. Power Sources* **2024**, *591*, 233875.
[20] Y.-N. Zhou, J.-J. Ding, K.-W. Nam, X. Yu, S.-M. Bak, E. Hu, J. Liu, J. Bai, H. Li, Z.-W. Fu, X.-Q. Yang, *J. Mater. Chem. A* **2013**, *1*, 11130.
[21] L. Zheng, J. C. Bennett, M. N. Obrovac, *J. Electrochem. Soc.* **2019**, *14*, A2058.
[22] S. Wang, F. Chen, H.-Y. He, Y.-R. Zhu, H.-B. Liu, C.-H. Chen, *J. Alloys compd.* **2022**, *925*, 166690.
[23] Y. Tsuchiya, A. M. Glushenkov, N. Yabuuchi, *ACS Appl. Nano Materials* **2018**, *1*, 364.
[24] J.-Y. Hwang, T.-Y. Yu, Y.-K. Sun, *J. Mater. Chem. A* **2018**, *6*, 16854.
[25] G. Oh, S. Kansara, X. Xu, Y. Liu, S. Xiong, J.-Y. Hwang, *Adv. Funct. Mater.* **2024**, *34*, 2401210.
[26] H. Hu, H. Chen, S. Xu, M. Zhou, X. Zhang, T. Shen, H. Li, H. Zhou, *ACS Appl. Energy Mater.* **2024**, *7*, 7397.
[27] L. Wang, Y.-G. Sun, J.-Y. Piao, A. Manthiram, J. Ma, A.-M. Cao, *J. Mater. Chem. A* **2017**, *5*, 8752.
[28] Q. Shi, R. Qi, X. Feng, J. Wang, Y. Li, Z. Yao, X. Wang, Q. Li, X. Lu, J. Zhang, Y. Zhao, *Nat. Commun.* **2022**, *13*, 3205.
[29] M. Boukriba, F. Sediri, N. Gharbi, *Mater. Res. Bull.* **2013**, *48*, 574.
[30] S.-H. Bo, X. Li, A. J. Toumar, G. Ceder, *Chem. Mater.* **2016**, *28*, 1419.
[31] X. Liang, X. Song, H. H. Sun, H. Kim, M.-C. Kim, Y.-K. Sun, *Nat. Commun.* **2025**, *16*, 3505.
[32] C. Ma, X.-L. Li, X.-Y. Yue, J. Bao, R.-J. Luo, Y.-N. Zhou, *J. Chem. Eng.* **2022**, *432*, 134305.
[33] Y.-T. Tsai, N. Majewska, M. Kamiński, B.-H. Lin, S. Mahlik, M.-H. Fang, *ACS Appl. Mater. Interfaces* **2023**, *15*, 49379.
[34] R. Berthelot, D. Carlier, C. Delmas, *Nat. Mater.* **2011**, *10*, 74.
[35] G. Oh, Y. Oh, S. Kansara, H. Shin, H. Kang, T.-H. Kim, D. Bresser, J.-Y. Hwang, *Small Struct.* **2025**, *6*, 2400561.
[36] B. Sambandam, S. Kim, D. T. Pham, V. Mathew, J. Lee, S. Lee, V. Soundharrajan, S. Kim, M. H. Alfaruqi, J.-Y. Hwang, J. Kim, *Energy Stor. Mater.* **2021**, *35*, 47.
[37] J.-Y. Hwang, S.-T. Myung, J. U. Choi, C. S. Yoon, H. Yashiro, Y.-K. Sun, *J. Mater. Chem. A* **2017**, *5*, 23671.
[38] J.-H. Kim, J.-M. Kim, S.-K. Cho, N.-Y. Kim, S.-Y. Lee, *Nat. Commun.* **2022**, *13*, 2541.
[39] S. Jeong, H. Kang, S. Ryu, G. Oh, Y.-C. Jung, C. Hwang, T.-Y. Yu, J. T. Kim, H.-G. Jung, Y.-K. Sun, J.-Y. Hwang, *ACS Appl. Mater. Interfaces* **2024**, *16*, 44737.
[40] M. Dahbi, T. Nakano, N. Yabuuchi, S. Fujimura, K. Chihara, K. Kubota, J.-Y. Son, Y.-T. Cui, H. Oji, S. Komaba, *ChemElectroChem* **2016**, *3*, 1856.
[41] J.-J. Fan, P. Dai, C.-G. Shi, Y. Wen, C.-X. Luo, J. Yang, C. Song, L. Huang, S.-G. Sun, *Adv. Funct. Mater.* **2021**, *31*, 2010500.
[42] S. Jia, S. Kumakura, E. McCalla, *Energy Environ. Sci.* **2024**, *17*, 4343.
[43] I. Lee, G. Oh, S. Lee, T.-Y. Yu, M. H. Alfaruqi, V. Mathew, B. Sambandam, Y.-K. Sun, J.-Y. Hwang, J. Kim, *Energy Stor. Mater.* **2021**, *41*, 183.
[44] Z. Lu, J. R. Dahn, *Chem. Mater.* **2001**, *13*, 1252.
[45] X.-G. Yuan, Y.-J. Guo, L. Gan, X.-A. Yang, W.-H. He, X.-S. Zhang, Y.-X. Yum, S. Xin, H.-R. Yao, Z. Huang, Y.-G. Guo, *Adv. Funct. Mater.* **2022**, *32*, 2111466.
[46] X. Lin, S. Zhang, M. Yang, B. Xiao, Y. Zhao, J. Luo, J. Fu, C. Wang, X. Li, W. Li, F. Yang, H. Duan, J. Liang, B. Fu, H. Abdolvand, J. Guo, G. King, X. Sun, *Nat. Mater.* **2024**, *24*, 83.
[47] C. K. Moon, H.-J. Lee, J. H. Park, H. Kwak, J. W. Heo, K. Choi, H. Yang, M.-S. Kim, S.-T. Hong, J. H. Lee, Y. S. Jung, *ACS Energy Lett.* **2018**, *3*, 2504.
[48] G. Kresse, J. Furthmüller, *Phys. Rev. B* **1996**, *54*, 11169.
[49] P. E. Blöchl, *Phys. Rev. B* **1994**, *50*, 17953.
[50] G. Henkelman, B. P. Uberuaga, H. Jónsson. *Chem. Phys.* **2000**, *113*, 9901.
[51] L. L. Wong, K. C. Phuah, R. Dai, H. Chen, W. S. Chew, S. Adams, *Chem. Mater.* **2021**, *33*, 625.
[52] S. Maintz, V. L. Deringer, A. L. Tchougréeff, R. Dronskowski, *J. Comput. Chem.* **2016**, *37*, 1030.
[53] S. Kansara, H. Kang, S. Ryu, H. H. Sun, J.-Y. Hwang, *J. Mater. Chem. A* **2023**, *11*, 24482.